UNIVERSITY OF AMSTERDAM

UvA-DARE (Digital Academic Repository)

A study on giant radio pulses

Karuppusamy, R.

[Link to publication](#)

Crab Giant Pulses

R. Karuppusamy, B. W. Stappers and W. van Straten

Abstract The pulsar embedded in the bright, young Crab supernova remanant is known for its giant pulse emission. Past studies have concentrated only on the very bright pulses or were not sensitive to the faint end of the giant pulse luminosity distribution. With our new instrumentation offering a large bandwidth and high time resolution combined with the narrow radio beam of the Westerbork Synthesis Radio Telescope, we seek to probe the weak giant pulse emission regime by a study of large population of giant pulses from the Crab pulsar. The analysis includes the distributions of the measured pulse widths, intensities, energies and scattering times.

The Westerbork Synthesis Radio Telescope (WSRT) was used in a phased array mode, resolving out a large fraction of the Crab nebula. The pulsar signal was recorded using the PuMa II pulsar backend and then coherently dedispersed and searched for giant pulses. After careful flux calibration, the data was analysed to study the giant pulse properties. The weak giant pulses are shown to form a separate part of the intensity distribution. The large number of giant pulses detected were used to analyse scattering and scintillation in giant pulses. We report for the first time the detection of giant pulse emission at both the main and interpulse phases within a single rotation period. The rate of detection is consistent with the appearance of pulses at either pulse phase as being independent. We use these pulse pairs to determine scintillation timescales within a single pulse period.

3.1   Introduction

The Crab nebula, identified as the supernova remnant which resulted from SN 1054, is one of the strongest radio sources in the sky and harbours the young neutron star PSR B0531+21. The pulsar is visible across the entire observable electromagnetic spectrum; at radio wavelengths it is the second brightest pulsar in the northern sky. PSR B0531+21 was discovered by Staelin & Reifenstein (1968), soon after the discovery of pulsars. The pulsar is noted for several features including the near orthogonal alignment of the magnetic and rotational axis that gives rise to the observed interpulse emission. The average emission profile of the pulsar, obtained by averaging the radio emission from many rotations of the star, exhibits a number of features that change quite remarkably with radio frequency (Moffett & Hankins 1994). The individual pulses show a large variation in amplitude and duration as a function of time. The most enigmatic of these are its occassional intense bursts known as giant pulses (Heiles et al. 1970; Staelin & Sutton 1970). The giant pulses can be extremely narrow – of the order of 0.4 ns (Hankins & Eilek 2007) – and the pulse flux can be several 1000 times the average pulse flux. The ultrashort durations of the giant pulses imply very high equivalent brightness temperatures (Hankins et al. 2003) indicate that it originates from a nonthermal, coherent emission process.

   The Crab pulsar is one of just a handful of pulsars which have been shown to have giant pulse emission. Some other pulsars, like the young Vela pulsar also show narrow, bursty emission called giant micropulses (Johnston et al. 2001). The fluxes of these micropulses are within a factor of 3 times the average pulse flux. In the pulsars that show giant pulse emission, the pulse intensity and energy distributions exhibit power-law statistics (Argyle & Gower 1972) while the giant micropulses give rise to log-normal distributions Cairns et al. (2001). In contrast the bulk of the pulsar population have pulse intensities and energies that are normally distributed (Hesse & Wielebinski 1974). This indicates that the giant pulses and micropulses may form a different emission population.

   The Crab giant pulses have been studied by various groups, yet the nature of the emission process remains elusive. In very early studies at low sky frequencies, the data was afflicted by dispersion smearing and scattering (Heiles et al. 1970; Gower & Argyle 1972), but the power law nature of the intensity distribution of giant pulses was identified. The next major study by Lundgren et al. (1995) discussed a multi-wavelength observation of giant pulse emission, and noted the possibility of a weak giant pulse emission population at radio wavelengths, which they were unable to resolve due to insufficient sensitivity. Sallmen et al. (1999) found that the Crab giant pulses are broad band at radio wavelengths. They also determined giant pulse spectral indicies in the range of -2.2 to -4.9 using their widely spaced observation bands and 21 simultaneously detected giant pulses. Observations by Hankins et al. (2003) revealed that giant pulses at 5.5 GHz contained nanosecond wide subpulses and the presence of such narrow features had been predicted in numerical modelling by Weatherall (1998). At these frequencies the radio emission character of the Crab pulsar changes, with the interpulse emission becoming dominant. A multi-wavelength radio observation of Crab giant pulses with widely spaced frequency bands (0.43 GHz and 8.8 GHz) was presented by Cordes et al. (2004), and they discuss the effects of scintillation over a wide range of frequencies. Popov

& Stappers (2007) and Eilek et al. (2002) investigated pulse width distriutions and found that narrow pulses tend to be brighter. Bhat et al. (2008) carried out a similar analysis in addition to scattering and dispersion variations in the nebula. All of these studies point to the peculiarity of the Crab pulsar and its puzzling emission process, and motivates further study at finer detail using a large number of pulses. For the work discussed in this chapter, we utilize the wide band capabilities of the new pulsar machine, PuMa–II described in Chapter 2 and the Westerbork Synthesis Radio Telescope (WSRT) in the coherent tied array mode. At small hour angles, the synthesized beam of the WSRT effectively resolves out the Crab nebula reducing the nebular contribution to the system temperature. Thus the WSRT and PuMa–II combination makes this study much more sensitive in terms of signal-to-noise ratio acheived, and number of pulses than was possible in the past. The rest of this chapter is organized as follows: in §2 we describe the observation set up and data reduction. Flux calibration is discussed in §3. The giant pulse characteristics are discussed in §4. We report detections of double giant pulses in §5 and the scattering analysis is presented in §3.6.

3.2 Observations and data reduction

The radio observations of the Crab Pulsar reported here were carried out as part of a multi-wavelength observation with the Integral γ-ray telescope and the WSRT on 11 October 2005. The WSRT observations were from UTC $03^{\rm h}56^{\rm m}50^{\rm s}$ to $09^{\rm h}36^{\rm m}20^{\rm s}$ with a break of three minutes in the middle of the observation to switch data disks. The results of the γ-ray observations will be reported elsewhere.

The pulsar was observed at eight different sky frequencies in the L–Band, which is the most sensitive front-end receiver at the WSRT (T_{sys} = 30 K). The sky frequencies (see Table.

Parameter	Value
Observation duration	21420 s
Start Epoch	53654.726505 (MJD)
Sky frequencies	1311[a], 1330, 1350, 1370, 1392[a]
	1410, 1428[a,b], 1450 MHz
Bandwidth	8×20 MHz
Nominal T_{sys}	30 K
Beam size	$21'' \times 1741''$ [c]

[a] These frequencies are not uniformly spaced to avoid interference.

[b] This band was not recorded due to disk failure.

[c] The beam size varies as a function of the observation time. See text for details.

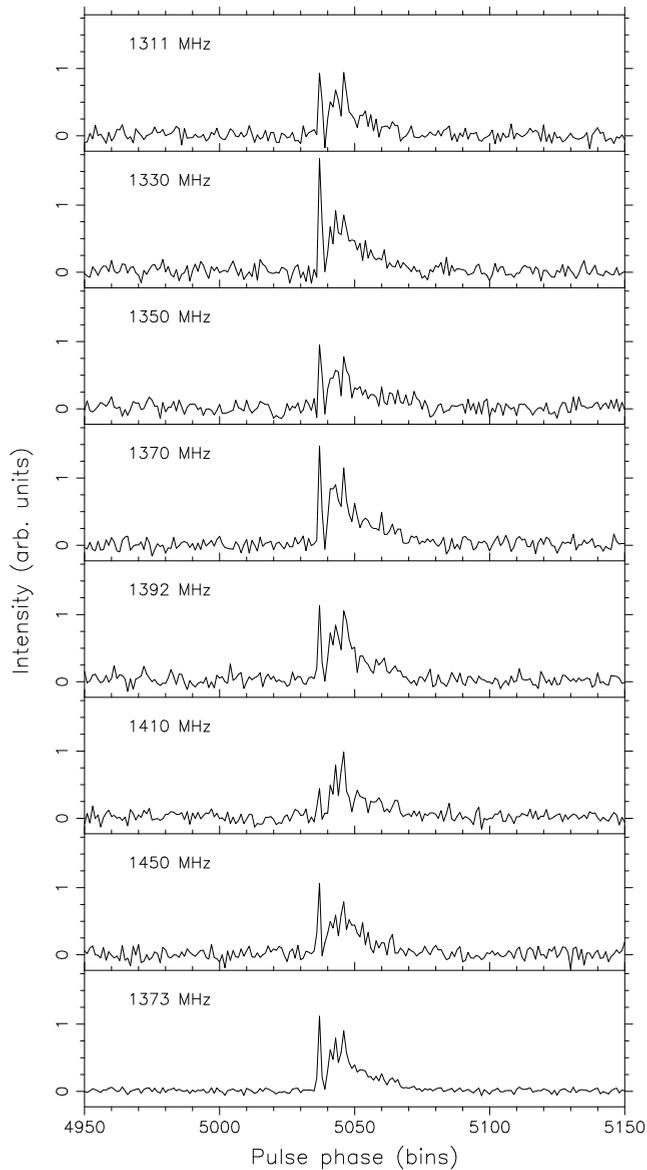**Table 3.1:** Telescope parameters and observation details.

Figure 3.1: Total intensity of a coherently dedispersed giant pulse at the main pulse phase detected in all recorded bands at 4.1 μs resolution. The total dispersion delay of 24.9 ms across the seven bands was removed for this plot. The lower most panel shows the pulse after combining the signal in all seven bands. The pulses displayed here are scaled relative to the pulse at 1330 MHz.
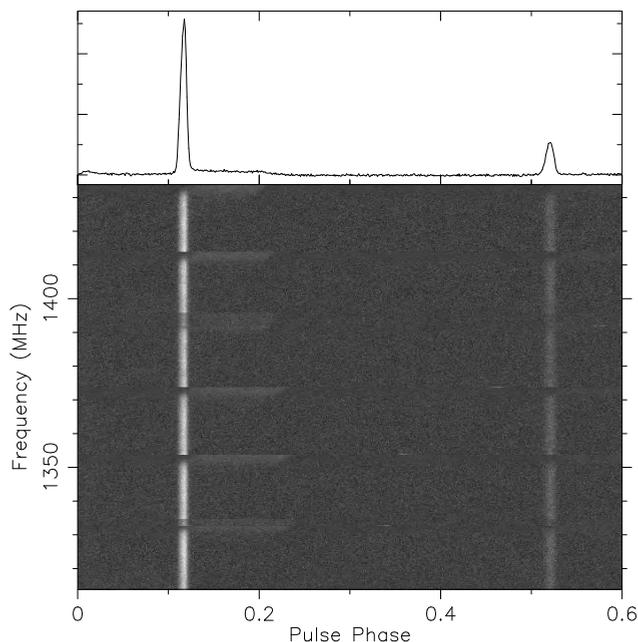
Figure 3.2: Total intensity plot for six of the seven recorded bands shown here after coherent dedispersion and combining in software. The striped nature of channels at 1330 MHz and 1390 MHz is due to the overlap in the adajcent frequency bands. The roll-off of the filters used in the system is also seen as a reduced intensity at the band edges. A low level extended feature is seen at the edge (also visible in the top panel as the elevated baseline in the right side of the main pulse) of each band which is due to the 2-bit quantization noise, and is visible only in long exposures.

3.1) were chosen to be free of radio frequency interference. Two orthogonal polarizations of 8×20 MHz analogue signals from each telescope were 2-bit sampled at the Nyquist rate of 40 MHz. The telescope was operated in the tied array mode in which coherent sums of the sampled voltages were formed in dedicated adder units resulting in 6-bit summed voltages. A coherent sum was achieved by determining the instrumental phase offsets between the telescopes using observations of a strong calibrator source. These phase offsets, combined with the geometrical phase offsets required for tracking the source are applied to each telescope. The resultant values were then read off as 8-bit data and recorded in the PuMa–II storage nodes. This resulted in a total of 13.5 Terabytes of raw data. After the observation the data were processed offline using the open-source pulsar data processing software package DSPSR[1]. A 32-channel synthetic coherent filterbank was formed across each 20 MHz band with coherent dedispersion applied across each of the channels using the dispersion measure (DM) of the pulsar. We obtained the DM (= 56.742) from the list maintained by the Jodrell

---

[1]http://dspsr.sourceforge.net/

Bank Observatory[2] (Lyne et al. 1993) at an epoch closest to our observation. Frequency resolution was preserved so that studies of spectral indices, scintillation and scattering could be carried out.

From the dedispersed data the total intensity was computed for each pulse. Giant pulses were detected by computing the peak signal-to-noise ratio denoted by S/N. The giant pulse detection threshold was set at $S/N \geq 7\sigma$ in each band, where σ is the off-pulse root-mean-square noise fluctuation. Pulses below the detection threshold were discarded to ease storage requirements. The signal was originally sampled at the Nyquist rate resulting in a time resolution of 25 ns. The 32-channel filterbank and the choice of 4.1 μs final time resolution resulted in 8192 phase bins. The time resolution of 4.1 μs was chosen to match the estimated scattering time scale available at the time (Sallmen et al. 1999). However, it is known from recent work by Bhat et al. (2008) that single pulses at these radio frequencies can be as narrow as 0.5 μs. In addition to the single pulses, average pulse profiles with 128 frequency channels in each 20 MHz band were formed every 10 seconds.

The reduced data consisted of ~21000 giant pulse candidates in each recorded band. An example candidate is shown in Figure 3.1, where the pulse was detected in all bands. In the offline analysis stage these candidates were combined in software using only pulses that show the expected dispersion delay. This method ensures that spurious signals are filtered out in our analysis. After combining in software, 12959 giant pulses were identifed to have occured simultaneously at all observed sky frequencies. Of the 12959 pulses, 11384 were detected at the main pulse phase and 1370 at the interpulse phase of the average pulse profile respectively.

Folding of the data and forming the single pulses was performed using the DSPSR software package and a polynomial determined by using TEMPO (Taylor & Weisberg 1989). The folded profiles formed in each 20-MHz band were combined in software to validate the DM used. The combined data is shown in Figure 3.2 as a frequency–phase image and shows no smearing, confirming that the value of DM is right. A similar procedure was used to combine simultaneous giant pulses in all seven bands. Some artifacts of the 2-bit systems of the individual telescopes are visible once the profile is summed for the entire six-hour long observation. The width of these artifacts match the dispersion smearing in the bands as seen in the top panel of Figure 3.2. The quantization noise is 12% for a single telescope, whose signal is sampled using 2-bits (Cooper 1970). Since signals from the 14 telescopes of the array were coherently summed, the uncorrelated quantization noise is reduced by a factor of $\sqrt{14}$. The resulting noise of 3.7% is considered too small to be problematic in the analysis that follows. In many stages of the analysis, extensive use of the PSRCHIVE (Hotan et al. 2004) utilities were made to view and validate the pulsar data and to compute the S/N used in further analysis.

---

[2]http://www.jb.man.ac.uk/ pulsar/crab.html

3.3 Flux calibration

To establish a flux scale for the observed giant pulses, the mean system flux needs to be computed. The mean system flux is proportional to the r.m.s noise variations at the telescope output and can be expressed by the radiometer equation (Dicke 1946),

$$S_{min} = \frac{S_{sys}}{\sqrt{N_p \cdot B \cdot T_{int}}}, \tag{3.1}$$

where, S_{min} is the r.m.s system noise in Jy, S_{sys} is the total system noise, N_p is the number of polarizations (= 2), B is the bandwidth in Hz (= 140 MHz) and T_{int} is the integration time in seconds.

The total system noise in flux density units in equation (3.1) is the total equivalent system temperature divided by the telescope gain ($S_{sys} = T_{total}/G$). For the WSRT, when signals from the fourteen 25-m parabolic dishes are combined, the resulting telescope gain[3] is $G =$ 1.2 K.Jy^{-1}. The term T_{total}, can again be expressed as,

$$T_{total} = T_{sys} + f_\nu(t) \cdot T_{cn}, \tag{3.2}$$

The term T_{cn} is the contribution of the Crab Nebula to the system temperature, while the term $f_\nu(t)$ is a time dependent factor explained below. Following Bietenholz et al. (1997), we express the total flux of the Crab Nebula at frequency ν (in GHz) as $S_{CN} = 955\nu^{-0.27}$, from which T_{cn} is computed. The WSRT is an east-west array and the coherent addition of the telescope signals results in a $21'' \times 1741''$ fan beam. The Crab nebula is an extended source of size $\Omega_{cn} = 6' \times 4'$. Hence the WSRT's fan beam resolves the Crab nebula in the east-west direction. This in turn reduces the nebular contribution to the T_{sys}. However, the width of the WSRT's fan beam is not a constant, but is a function of the observation time. As the source is tracked in hour angle, the effective width of the synthesized beam can be expressed as $\Omega_A(t) = \Omega_{cn} \cdot \lambda/D \cdot cos(HA)$. In this expression $HA = t - RA$, where t is the local sideral time, the maximum baseline $D = 2700m$ and RA is the right ascention of the Crab pulsar. The fraction of the nebular contribution can be expressed as $f_\nu(t) = \Omega_A(t)/\Omega_{cn}$, which reaches its minimum value of 0.13 at zenith. As the source is tracked toward the horizon, the projected distance between the dishes decreases and $\Omega_A(t)$ increases. Consequently, the observing system becomes less sensitive toward larger hour angles, or when the source rises and sets. This time dependence of the system noise is included in our flux calibration. The variation of S_{min} is shown for a bandwidth of 140 MHz, $N_p = 2$ and $\tau = 4.1\ \mu s$ in the upper panel of Figure 3.3. A plot of the pulse intensity during the observation (lower panel of Figure 3.3) confirms this reduction in sensitivity.

The peak flux of the giant pulses were computed using the modified radiometer equation (Lorimer, D. R. and Kramer, M. 2005) for the pulsar case, $S_{peak} = (S/N) \cdot S_{min}$. With the above considerations of the nebular contribution to T_{total} and with $T_{sys} = 30K$ in the WSRT's L–Band, the system retained good sensitivity in the first 15000 seconds of the observation.

---

[3]The telescope gain is 1.34 K.Jy^{-1} for an ideal array combiner. The reduction in gain is attributed to losses in the formation of the tied array signal.
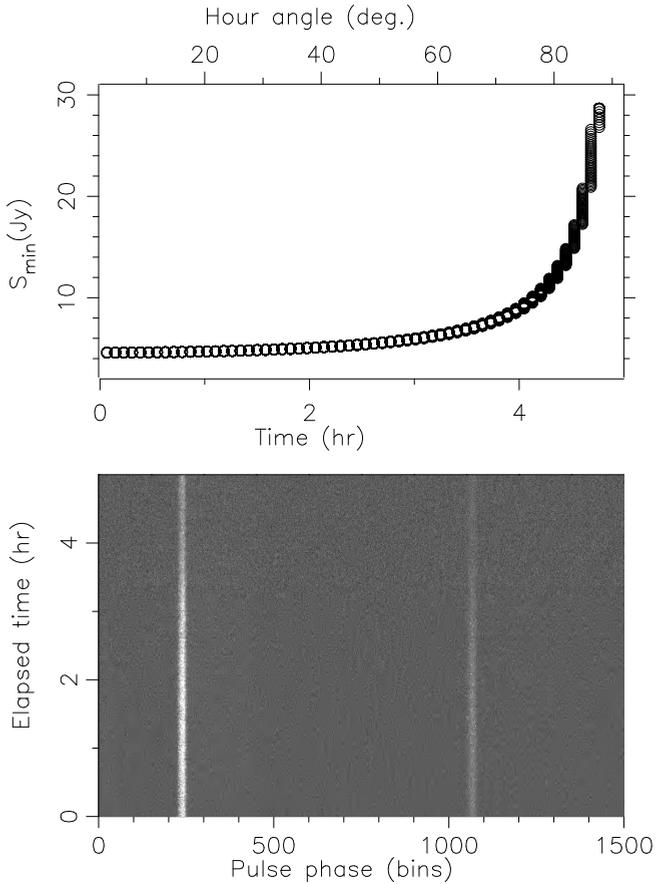
Figure 3.3: The upper panel shows the change in minimum detectable signal S_{min} within a 4.1 μs time interval during the first 5 hours of the 6-hour observation. The hour angle of the source is displayed in the top ordinate axis. The lower panel is the observed change in peak signal-to-noise ratio of the detected signal. The dependence of the signal-to-noise ratio on the hour angle of source is discussed in the text.

Two other factors have been neglected in this calibration procedure which do not contribute significantly to the T_{sys} : the relative change of the orientation of the WSRT's fan beam and the Crab nebula over the course of observation and the partial shadowing of three telescopes out of the 14 for HA > 54° (the last 3 hours of our observation).

3.4 Single pulse statistics

For the analysis that follows, all pulses that were flux calibrated as described in the previous section were used. The discussed change in system sensitivity does not limit this analysis due to our careful flux calibration procedure. While approximately 70% of the pulses were detected in all seven bands simultaneously, the rest were detected in two or more of the seven bands recorded. For the results described below, where applicable, only those pulses that were detected in all seven bands were used and explicitly mentioned.

3.4.1 Pulse intensity distributions

The giant pulse fluxes of the Crab pulsar contribute to the long exponential tail of the single pulse intensity histograms (Argyle & Gower 1972), while the normal pulsar population show pulses which have Gaussian intensity distributions (Hesse & Wielebinski 1974). Figure 3.4 shows the average pulse flux distribution for pulses detected in at least two of the seven recorded bands. The average pulse flux is computed by integrating all emission within the equivalent width, W_{eq} of the giant pulse (see §3.4.4). This value is averaged over the pulse period to obtain the average pulse flux. The pulse in each band was detected based on a threshold of 7σ. A pulse detected in two bands satisfies $\sqrt{2}\times7 = 9.89\sigma$ limit. In the first three hours of the observation (when the system was most sensitive), the flux equivalent system noise in 4.1 μs is 109 Jy. Averaged over the pulse period, a pulse of $S/N = 9.89\sigma$ corresponds to an average pulse flux density of 3.9 Jy. Hence, the flux distribution computed here contains a good fraction of weak giant pulses compared to those reported elsewhere (see Table. 3.2). The tail of the distribution is well described by a power law curve, $N_F \propto F^\alpha$, where N_F is the number of pulses detected in 1.8 Jy flux intervals of F. The value of $\alpha = -2.79 \pm 0.01$ and $\alpha = -3.06 \pm 0.06$ was determined from the best fits to the data in the interval 118 Jy $\leq F \leq$ 2000 Jy and 40 Jy $\leq F \leq$ 596 Jy for the giant pulses in the main and interpulse respectively.

Reference	Frequency (MHz)	Threshold (Jy)
Lundgren et al. (1995)	800	120.0
Popov & Stappers (2007)	1197	5.9 [a]
Bhat et al. (2008)	1300/1470	22.3 [b]
This chapter	1373	3.9

[a] Equivalent average pulse computed flux from the quoted 6σ peak flux density of 142 Jy, assuming 0.036 pulse duty cycle.

[b] Average pulse flux density extrapolated for 7σ threshold, 4.1μs time resolution and pulse duty cycle ≈ 0.036.

Table 3.2: Reported sensitivity to the Crab giant pulse observations in the literature.
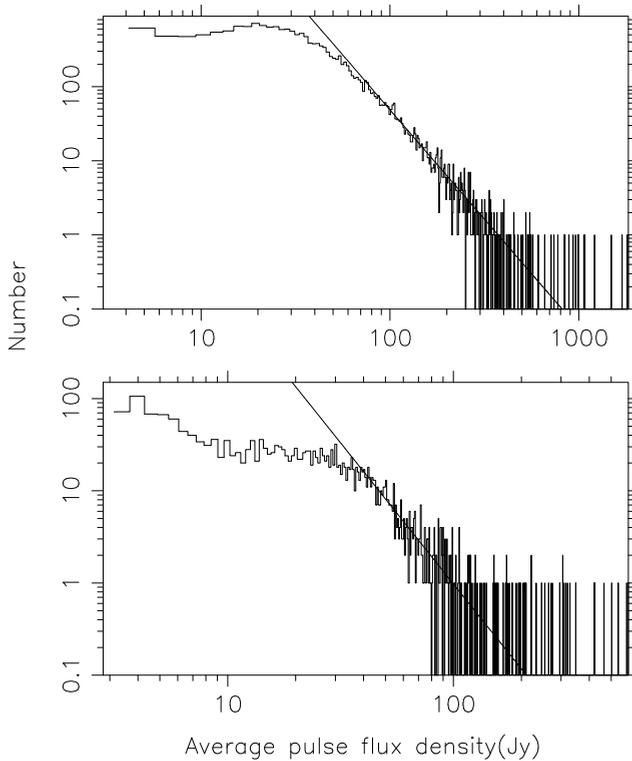
Figure 3.4: Distribution of the pulse intensity of all giant pulses detected at the main and interpulse phases in the upper and lower panels, respectively. The long tail results from the giant pulse emission. The best fit power law curve is shown with slope -2.79 ± 0.01 for the pulses in main pulse phase and -3.06 ± 0.06 for the pulses in the interpulse phase. The excess seen near 3Jy is due to rounding off in W_{eq}. [*see text for details*].

It is worth noting the differences in the intensity distributions displayed in Figure. 3.4. While the distribution of the giant pulses in the main pulse phase shows a clear turn over at ~20 Jy, the emergence of a bimodality in the region containing weak pulses is evident in the intensity distribution of the interpulse giants. The weak giant pulses and the normal pulses convolve giving rise to this bi-modal distribution. The distribution corresponding to the interpulse phase also shows a flattening in the 10–30 Jy region. The clear excess of weak pulses in both the distributions in the region $F \leq 5$ Jy is due to our method of setting $W_{eq} = 4.1~\mu s$ (equal to the time resolution). In this case the emission window considered is dominated by noise or weak and narrow pulses. The slopes of the power law models obtained here can be compared to the values reported earlier. Figure 4 of Lundgren et al. (1995) shows for data at 800 MHz, a slope of -3.46 ± 0.04. Cordes et al. (2004) derived a value of ~ -2.3 at 433 MHz and Bhat et al. (2008) found -2.33 ± 0.14 at 1300 MHz. The value of the slope of the power law fit to the main pulse intensity distribution reported here is in general agreement

considering the effect of low number statisics and/or dispersion smearing in the observations reported elsewhere. We note that while this experiment was sensitive to much lower fluxes, the long observation time has also enabled the detection of rarer bright pulses.
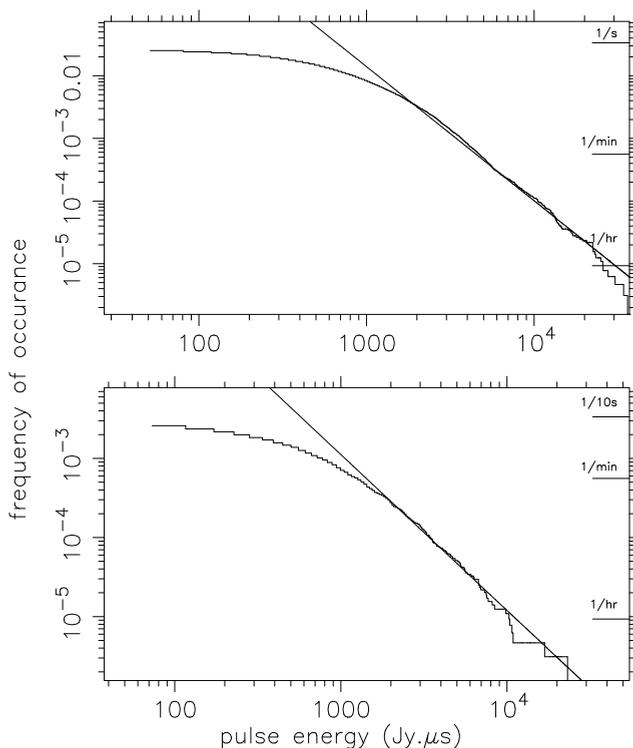
3.4.2   Pulse energy distributions

Figure 3.5: The cumulative probablity distribution of the energy in giant pulses detected at the main pulse and the interpulse phases in the upper and lower panel, respectively. The y-axis is the fraction of the total number of pulses and pulse energy is plotted on the x-axis. Also shown are the occurance rates per minute, second and hour.

The relative occurance rates of giant pulses is displayed as a cumulative probablity distribution of the individual pulse energies in Figure 3.5. The pulse energy is computed by multiplying the equivalent width, W_{eq} and the average pulse flux. As described in §3.4.1, we computed the best fits to the cumulative probablity distributions of the main and interpulse giants. The power law curve with $\alpha = -2.13 \pm 0.007$ and $\alpha = -1.97 \pm 0.006$ fits the data well for pulse energies at the main and inter pulse phases, respectively. The break seen at ~2000 Jy.μs is consistent with the break value reported by Popov & Stappers (2007). We note that the emission at the interpulse phase shows a somewhat shallower power law.

It is known from Popov & Stappers (2007) that the power law index has a width dependence, varying from -1.7 to -3.2 as the pulse width increases. Based on this variation, the index we find is in good agreement with Popov & Stappers (2007) and Bhat et al. (2008) (-1.88 ± 0.02 at 1300 MHz). However, we fit only a single power-law unlike the two power-law fits found by these authors. Partial fits to the low energy pulses yield more than two components, with shallower power law indicies indicating a simple dual-component fit is insufficient. One explanation for this can be the bias introduced by setting $W_{eq} = 4.1\ \mu s$ for narrow pulses, overestimating the pulse energy. However this can only be a minor contribution and argues that there is a clear break in the intensity distribution. To compare the occurance rates we see here, we proceed to derive the rates from the arrival times of the giant pulses in the next section.

3.4.3   Giant pulse rates

The distribution of the separation times between successive giant pulses is plotted in Figure 3.6. If the giant pulses are mutually exclusive events independent of each other, then the arrival time separation follows a Poisson process (Lundgren et al. 1995). The probablity of a giant pulse occuring in the interval x is then given by $P(x) = \mu x.e^{-\mu x}$, where μ is the mean pulse rate. Since our data consists of only giant pulses, we expected to see an exponential reduction in the separation time between the pulses. Figure 3.6 shows the fits to the separation times at both the inter- and main pulse phases.
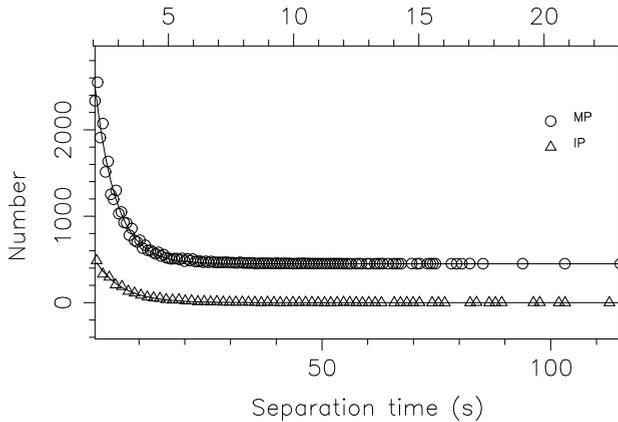

Figure 3.6: The symbols show the distribution of separation times between successive giant pulses at the main and interpulse phases and the solid lines are the best fits to the distribution. The top ordinate axis corresponds to the curve and data for the pulses at the main pulse phase and are offset by 450 for clarity.

Functions with an exponential decay with time constants $1/\tau = 1.1 \pm 0.02$ and $1/\tau = 0.172 \pm 0.003$ are in excellent agreement with the data at the main and interpulse phases respectively. From the values of τ, the mean giant pulse rates are: one main pulse giant every

0.9 seconds and one inter pulse giant every 5.81 seconds observed above our threshold limit of 3.9 Jy. At these frequencies, the interpulse giants are comparatively less numerous as evident from our data. For comparision, in frequency bands above 5.5 GHz, the inter pulse giants are brighter and more frequent (Cordes et al. 2004). The combined rate of the giant pulses (fit and data not shown) is one pulse every 0.803 seconds. The foregoing discussion confirms earlier predictions that the giant pulse rate increases with frequency for the Crab pulsar (Lundgren et al. 1995; Sallmen et al. 1999). The effect of the WSRT's sensitivity reduction towards the end of the observation, as displayed in Figure. 3.3, may have contributed to the long tail of the distribution, where fewer pulses were detected in comparision to the first half of the observation. However, the rate derived here is robust, since the system had a good sensitivity in the first half of the observation.

3.4.4 Width distributions

The equivalent pulse width, W_{eq} is defined as the width of a top-hat pulse with height equal to the peak intensity of the pulse. W_{eq} for the giant pulses detected in all seven bands was computed. The results are displayed in panels on the right in Figure 3.7. We express W_{eq} as,

$$W_{eq} = \frac{1}{I_{max}} \times \sum_{i=n_1}^{n_2} I_i \times 4.1 \ \mu s \quad (3.3)$$

where I_{max} is the peak intensity, and I_i is the intensity in the pulse emission window defined by bins $i = n_1..n_2$ and is equal to 1ms in our case. Thus W_{eq} can be viewed as the equivalent width of a rectangular pulse in μs that has the same area as the giant pulse, with height I_{max}.

The giant pulses at these frequencies can be quite narrow. For instance, Bhat et al. (2008) found pulse widths to be 0.5 μs and (Eilek et al. 2002) found 0.2 μs. Our method of data reduction allowed a time resolution of 4.1 μs and therefore pulses with $W_{eq} < 4.1\mu s$ were taken to have a width equal to 4.1 μs. This results in some pulses being underestimated in flux and overestimated in equivalent width. The computed equivalent widths range from 4.1 μs to ~120 μs and we find that bright pulses tend to be narrow as seen in the left side panels of Figure 3.7. This was also suggested by Sallmen et al. (1999) and shown by Eilek et al. (2002). Popov & Stappers (2007) found a similar behaviour in addition to a width dependent break in the power law fits to the pulse energy distribution.

In the seven closely spaced radio bands observed, we note that a vast majority of the pulses have widths larger than 4.1 μs. This is seen in the pulse width histograms at the two pulse phases, displayed in the panels on the right in Figure. 3.7. The distribution shows a peak at ~16 μs, which is 4 times our ultimate time resolution in the main pulse and the peak shifts towards narrower timescales for the interpulses. We find less than 9% of the pulses with $W_{eq} = 4.1 \ \mu s$, indicating that the majority of the pulses show widths wider than our time resolution. The shape of the width distribution is similar at the both the main and interpulse phases.The contribution to the tail region of the distribution comes from scatter broadened pulses.
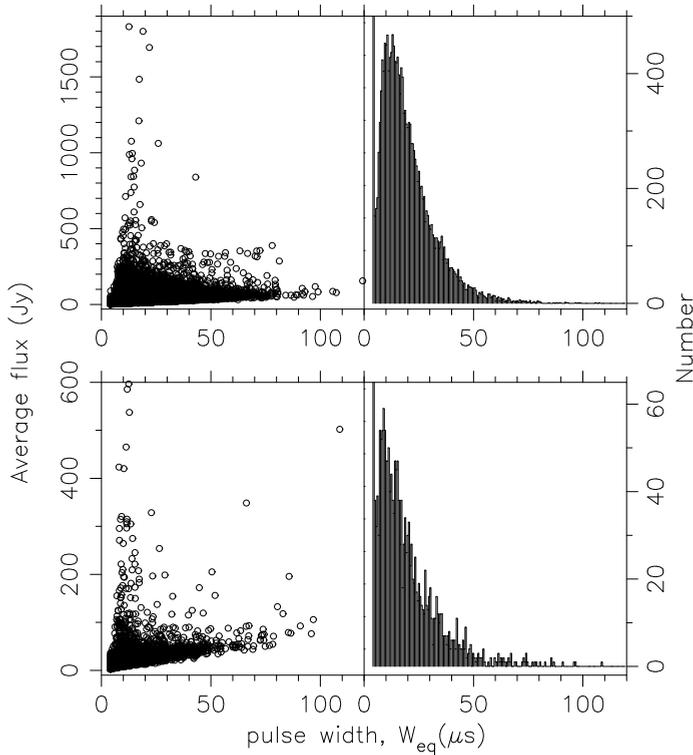
Figure 3.7: Plot of intensity against pulse width for the main and interpulse windows in the top left and lower left panel. A histogram of equivalent pulse widths in the top right and lower right panel. The distribution has an exponential envelope. For pulses with computed $Weq < 4.1 \, \mu s$ due to random noise fluctuations the widths were rounded off to $4.1 \, \mu s$.

3.4.5   Spectral index of giant pulses

The data were recorded in 7 different radio bands each 20 MHz wide in the frequency range 1300–1450 MHz; several thousands of pulses were detected simultaneously in all bands. The spectral index of individual pulses was computed by modelling the flux variation of a giant pulse as $S(\nu) \propto \nu^k$. $S(\nu)$ is the flux of the giant pulse at frequency ν, and k is the spectral index. The histograms of the derived spectral indices are displayed in Figure 3.8 for the giants at both pulse phases. A large dispersion in the spectral index is seen, with values -1.44 ± 3.3 and -0.6 ± 3.5 for the main and interpulse giants respectively.

These spectral index values are quite a bit shallower than those detected previously (see Introduction) over wider frequency separations. We therefore consider the effects of diffractive interstellar scintillation (DISS) on the spectral index estimates. Strong DISS results in pulse intensity variations within each of the seven bands. The effect of scintillation is to modulate the observed pulsar signal in both time and frequency. This is seen as regions of
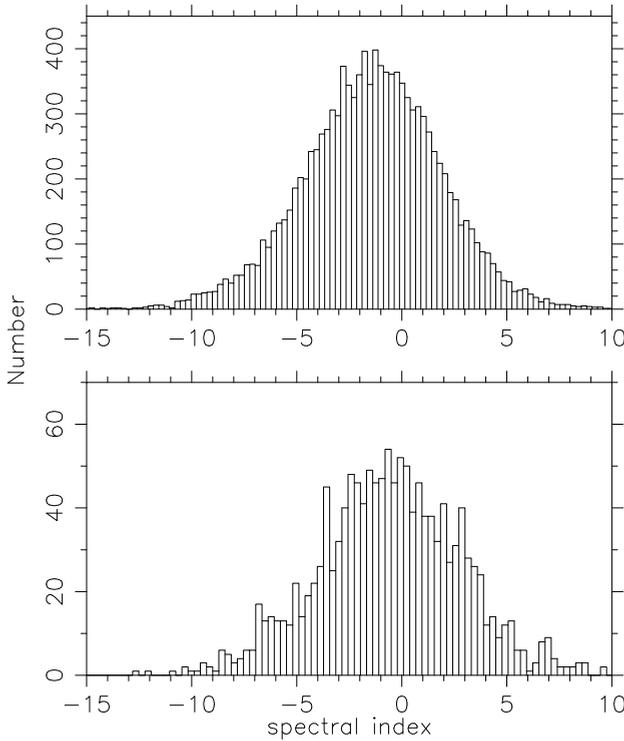
Figure 3.8: Histogram of spectral indices for the giant pulses detected at the main pulse (bottom panel) and the interpulse phase (top panel). The spread in the distributions is indicative of fitting errors. See text for details.

enhanced or diminished brightness in a grey scale plot of the intensity as function of time and frequency. These regions are known as scintiles. We estimate the scintillation bandwidth based the pulse scatter timescales, $\tau_s = 395 \pm 50 \mu s$ at sky frequency of 200 MHz, reported in the work of Bhat et al. (2007). We further make use of their revised $\tau_s \propto \nu^{-3.5}$ frequency scaling and that the scintillation bandwidth and scattering timescale are related by $2\pi\Delta\nu_d\tau_s = C_1$, where the constant $C_1 = 1.05$ for a thin scattering screen (Cordes et al. 2004). From these considerations $\Delta\nu_d \approx 0.25$–0.38 MHz in the 1300–1460 MHz band. On examining a few giant pulses by eye, it was clear that some of the scintiles are resolved while some were narrower than our channel width of $\Delta\nu = 0.625$ MHz. Thus, in the flux obtained by integrating the signal in the 20MHz-wide bands, the scintiles tend to average out. This implies that scintillation does not cause the spread in the spectral indicies of individual giant pulses. Moreover, with such narrow scintillation bandwidths, averaging over many giant pulse spectral index determinations as we have done here would expect to give an average spectral index which reflects the true average spectral index.

We note that refractive interstellar scintillation (RISS) cannot corrugate the spectra of sin-

gle pulses, since the pulse intensity variations due to RISS are only noticeable in observation on the order of a few days (Lundgren et al. 1995). However, the pulses do have significant structure intrinsic to the emission process. One example is displayed in Figure. 3.1 and these pulses do contribute to the spread in the computed spectral indicies. In this figure, it is clear that the leading short burst shows considerable variation across the seven bands, while the scattered trailing part of the pulse is correlated across frequency. This is again similar to what Hankins & Eilek (2007) found, as shown in their Figure 4, but at much higher frequency of ~9 GHz.

Sallmen et al. (1999) found that the spectral index variation is between −4.9 and −2.2 based on 29 pulses they observed in two bands centred at 1.4 GHz and 0.6 GHz. The spread in the indicies compute here and that of Sallmen et al. (1999) points to the stochastic nature of the giant pulse emission process and/or the disturbed plasma flow in the magnetosphere caused by strong plasma turbulence (Hankins & Eilek 2007). The giant pulses used in this analysis were detected in all seven bands which is 70% of all detected pulses in our data. Since each of our bands are 20 MHz wide, detection in seven bands implies an emission bandwidth of at least $\Delta v = 140$ MHz. This suggests that the emission bandwidth of Crab pulsar giants is potentially larger than $\Delta v / v = 0.1$, unlike the giant pulse emission from the millisecond pulsar B1937+21 (Popov & Stappers 2003). We detected a total of 17587 giant pulses, of which approxmiately 4000 were detected in less than 7 bands. Clearly it is not possible to include the pulses detected in only a few bands in this analysis as that would increase the dispersion in the spectral indicies computed. However this lack of detection in all bands, for pulses which were clearly detected in the other bands, argues that there are some narrow band effects which appear to modulate the giant pulse intensity.

3.5   Double giant pulses

During direct inspection of some giant pulses it was noticed that there were occassionally giant pulse emission seen at both the main and interpulse phases within a single rotation period of the star. To determine how many such pulses there are employed a search algorithm as follows: First, the giant pulses detected in all seven bands are combined in software across the frequency bands; The pulses are then averaged over polarisation and frequency to create a single pulse total intensity profile. The search algorithm was made sensitive to emission at both pulse phases by traversing each pulse profile twice; in the first pass, the emission peak and phase information is recorded, following which a search is made for any emission at the orthogonal pulse phase. All pulses that show signal $\geq 5\sigma$ in the second emission window are collected separately. The pulses returned by the search procedure were examined by eye to validate the double pulse nature. To our knowledge, this is the first instance that this phenomena is being reported. A total of 197 pulses that show emission at both pulse phases were found in our data set above the 5σ detection threshold.

To consider how likely this is to happen by chance, we note that the observation lasted 643263 rotations of the star and 11584 and 1375 pulses were found at the main and interpulse phases, respectively, above the 7σ detection threshold in each band. Since these giant pulses were detected in all seven bands, the effective threshold is now $\sqrt{7} \times 7\sigma = 18\sigma$. If the
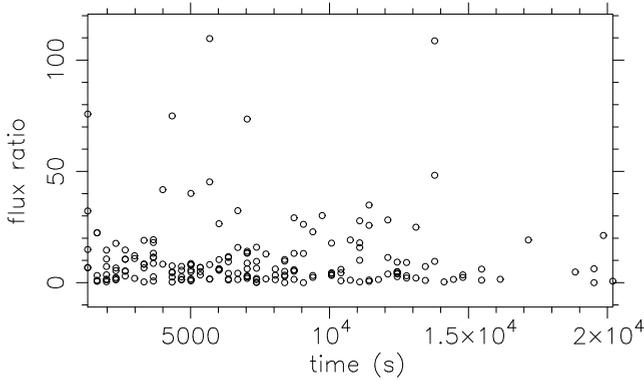
Figure 3.9: Detected double giant pulses shown as a ratio of the main pulse to the interpulse flux. On the x-axis, time since the start of the observation is shown.

18σ criterion is used to search for the double pulses, a total of 17 pulses are seen. In other words, only 17 pulses in the 197 detected show $S/N \geq 18\sigma$ at the orthogonal phase. Let the giant pulses occuring at the two pulse phases be mutually exclusive events, with individual probablitites $P(A)$ and $P(B)$. The chance of two giant pulses occuring within a single rotation period is the joint probablity $P(A, B) = P(A).P(B)$. Thus the chance of detecting a giant pulse above the 18σ threshold limit at the main and interpulse phases are $P(A) = 11584/643263$ and $P(B) = 1375/642263$ leading to $P(A, B) = 3.5 \times 10^{-5}$. Hence, we expect to see a total of $P(A, B) \times 643263 = 24$ pulse periods with pulses at both phases should be present in our data. The detection of 17 pulses is thus consistent with the expected 24 pulses.

Combining the seven bands improves sensitivity and allows the detection of weaker pulses. Considering pulses with S/N larger than 5σ in the orthogonal pulse phase within the double pulses resulted in the detection of an additional 180 double pulses. While the 197 pulses detected are not sufficient to perform meaningful statistics of these pulses, in § 3.6.1 we use our population of double giant pulses to study scintillation and scattering within a 0.5 rotation of the pulsar.

Although the appearance of the pulses in the same rotation period is consistent with the indivdual occurance rates we compared the GP properties at each phase. In the double pulses, the emission in the interpulse phase is typically narrower ($W_{eq} \lesssim 16\,\mu s$) than the emission at the main pulse phase and pulses at the main pulse phase are typically brighter, as shown in Figure 3.9. In both cases this is consistent with the known population of GPs at each phase. A similar analysis to §3.4.3 was done to determine the rate of double pulses and a rate of 1 pulse in 84 seconds, or one in 2545 rotations of the star was found to have giant pulse emission at both pulse phases. Thus, given the narrowness and very low occurance rates of these pulses, they were easily missed in earlier observations.

3.6   Single pulse scattering

The frequency resolution and large bandwidth of our data benefits scattering and scintillation checks on the individual pulses in two ways. First, the pulses detected in 7 bands are combined in software to give 224 channels across the 140 MHz bandwidth allowing examination of scintillation. Second, the large bandwidth of the combined pulse increases sensitivity and makes it possible to identify low level extended scatter tails. To characterise the scattering time τ_s in the interstellar medium, we computed the extent of pulse broadening in the individual giant pulses. The pulses can be described by a function with a vertical rise and an exponential decay to the data and is defined by,

$$f(t) = \begin{cases} e^{-t/\tau_s} & \text{if } t \geq 0 \\ 0 & \text{if } t < 0. \end{cases} \qquad (3.4)$$

This model is appropriate for a pulse scattered by a thin scattering screen located between the observer and the pulsar (Williamson 1972). It is known from the work of Sallmen et al. (1999), that a single one-sided exponential is not sufficient to model the complex structure of the giant pulses at this frequency. However, a large number of pulses in our data show a single exponential model fits most of the detected pulses within 10% error. Therefore, we proceeded with the single exponential fits. The value of τ_s obtained from the model fits are shown in the upper panel of Figure 3.10 as a function of observation time. The reduction in the scattering time towards the end of the observation is consistent with scattered pulses tending to be dimmer and therefore below the detection threshold. Only sufficiently bright pulses are detected in the sensitivity limited part of the observation, as discussed in §3.3. The scatter tail is also not discernible from the system noise in this part of the observation, limiting the determination of τ_s.

The distribution of the scattering times shows an exponential envelope, as seen in the lower panel of Figure 3.10. The individual pulse scattering time varies from $4.1\,\mu s$ to ~$90\,\mu s$. The large number of pulses in the distribution with $\tau_s \approx 4\,\mu s$ is related to our ultimate time resolution of $4.1\,\mu s$. This also implies that a large fraction of the pulses have scattering time $\tau_s \leq 4.1\,\mu s$. At an epoch slightly earlier than our observations, Bhat et al. (2007) determined a value of $\tau_s = 395 \pm 50\,\mu s$ at 200 MHz. Using their revised frequency scaling of $\tau_s \propto \nu^{-3.5\pm0.2}$, the scattering time at centre our band (1373 MHz) is $0.47 \pm 0.05\,\mu s$. At a slightly later epoch, Bhat et al. (2008) found a value of $\tau_s = 0.8 \pm 0.4\,\mu s$ at 1300 MHz which contrasts with the value of 8ms at 111 MHz (or $1.4\,\mu s$ at 1300 MHz using a $\nu^{-3.5}$ scaling law) reported by Kuzmin et al. (2008). With our data, we are not sensitive to scatter times less than $4.1\,\mu s$, but the dispersion seen in the histogram of scatter times in Figure. 3.10 shows that variations can be expected even within a single observation of six hours. We again refer to Figure. 3.1 for an example of the extreme form this variation: the different parts of the *same* pulse show different scattering effects, imparting significant structure to the pulse. In their work on DISS, Cordes & Rickett (1998) emphasize that considering the $1/e$ time equal to τ_s is valid only for a thin screen and does not always hold. In light of the limited validity in interpreting the $1/e$ time and the spread in the values of scatter times found in our analysis, we suggest that the scattering in the direction of Crab pulsar cannot be modelled by single thin screen. The Crab
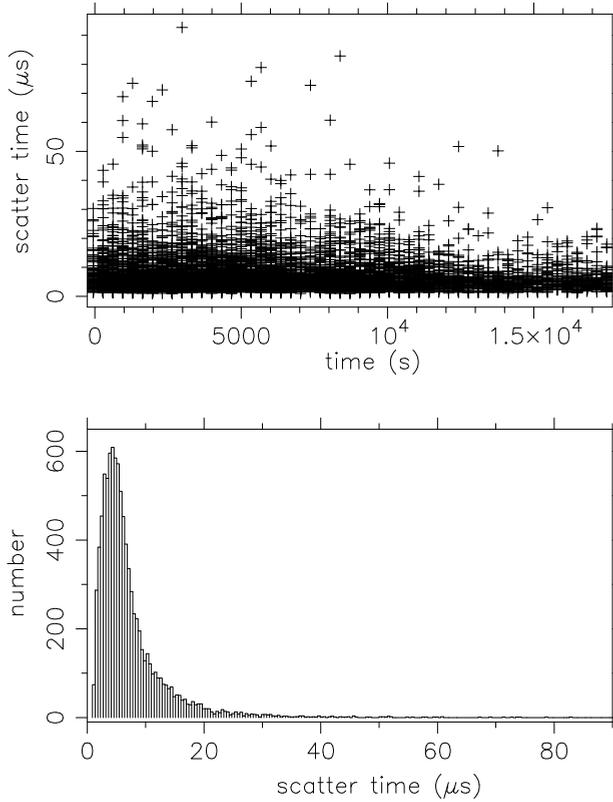
Figure 3.10: The upper panel shows a plot of the values of time constant τ_s from the fits to the scattering in the entire duration of observation for those pulses detected at the main pulse phase. The lower panel displays a histogram of the time constants obtained from exponential fits to the scatter tails of individual pulses. The values of $\tau_s \leq 4.1$ μs are those pulses narrower than our time resolution and are likely to be free of scattering.

nebula can clearly give rise to a complex screen or changes in the structures in the vicinity of the pulsar that give rise to the short term changes in scattering time (Backer et al. 2000; Lyne et al. 2001; Sallmen et al. 1999).

The diffractive scintillation timescale, Δt_{DISS} at this frequency was estimated by Cordes et al. (2004) as 25.5s, based on pairs of single pulses with sufficient S/N. However, the pulse pairs they used were separated in time by a few pulse periods. Since our data has good frequency resolution (224 frequency channels in 140 MHz), and we detected several pulses with multiple components, we proceeded to estimate possible variations of the scintillation time on shorter timescales.

3.6.1 Scintillation within single pulses

The scintillation timescale within single pulses were estimated using those pulses that show well separated components and the double pulses discussed in §3.5. The search for at least two components in single pulses was carried out based on the component separation of $\sim$25 μs. This was done by examining the pulses by eye, after an automated first pass. The first pass provided 451 giant pulse candidates and 368 of those displayed at least two distinct shots in the main pulse phase, and 18 candidates were found in the interpulse phase. The 197 double pulses were included in this analysis. Assuming that the two shots of pulses are intrinsic to the pulsar emission, and that the scattering screen remains stable within a pulse period, any scintillation would affect the two components similarly, introducing a correlated frequency structure. The scintillation timescale is then the $1/e$ point along the time axis of the 2-dimensional intensity correlation function, $C(\delta\nu, \tau) = \langle I(t, \nu).I(t+\tau, \nu+\delta\nu)\rangle$ of the spectrum (Cordes 1986). The computed correlation coefficients between the two components and the double pulses are displayed in Figure. 3.11.

The correlation coefficient of $\sim$0.4 for a large number of pulse component pairs is in excellent agreement with the value derived by Cordes et al. (2004). They derive a value of 0.33 considering the giant pulses to be 100% polarized, amplitude modulated, scintillated shot noise. It also implies that these components have undergone similar scintillation effects ruling out the possibility of any variation in the scattering medium on these timescales. The average correlation coefficients computed for the double pulses is consistent with the average value computed for the widely spaced pulse components (pulses in the top panel of Figure 3.11). Since a clear roll-off in the values of correlation coefficient is not seen in the data presented here, we conclude that the scintillation timescales are larger than 14 ms entirely consistent with Cordes et al. (2004).

3.7 Discussion

To our knowledge this is the largest collection of high time resolution giant pulse analysis presented in the literature. Even though some features of the giant pulse emission like the giant nano shots are in the process of being explained (Hankins & Eilek 2007), several questions still remain on the pulsar emission mechanism in general and the giant pulse phenomena in particular. From the measured pulse widths and the observed structure in many pulses, it is evident from the analysis presented in this chapter that the giant pulse emission is a manifestation of temporal plasma changes in the pulsar magnetosphere. The observed giant pulses rate is further evidence for this temporal variation, because if the mechanism responsible for the giant pulses is active on timescales longer than a pulse period, a clear excess of giant pulses separated by a single rotation period can be expected. On the basis of the giant pulse arrival times, it was concluded that the observed giant pulse emission is not due to a steady emission beam loosely bound to the stellar surface (Lundgren et al. 1995; Sallmen et al. 1999). We confirm that our data does not support such a model. For if such a beam with random wobbles operates, a characteristic width in the giant pulses can be expected. In other words, the distribution of the pulse widths would be normally distributed with a mean width.
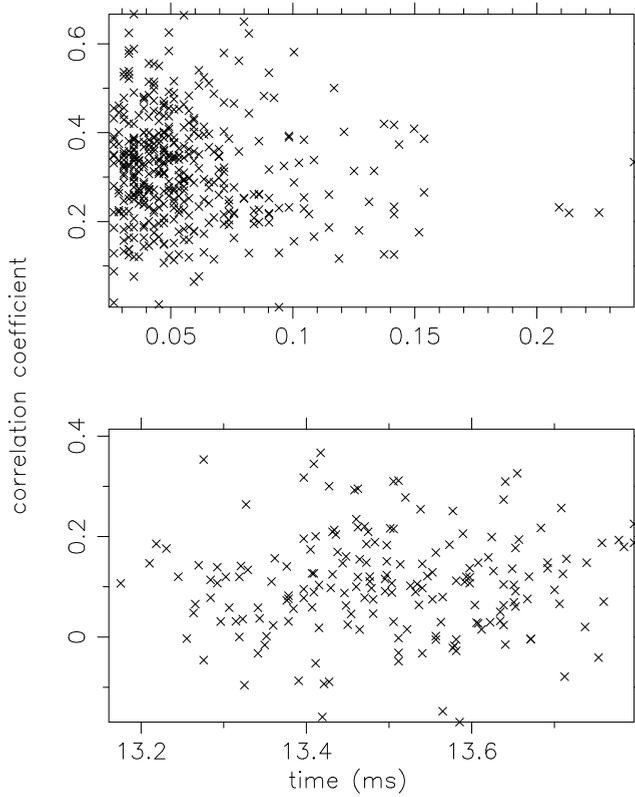
Figure 3.11: Correlation coefficients of the spectra within a single pulse period. Top panel shows correlation between the two components of giant pulse, while lower panel is the double giants. The separation between the components τ is shown in the abscissa.

The pulse intensity distributions have shown conclusively that the giant pulses consists of two distinct populations especially for those pulses found at the inter pulse phase. While there is evidence of a broadening of the pulses as they weaken in intensity they don't appear to be as broad as standard subpulses. In the model derived by Petrova (2004), a clear power law in the intensity distribution of the giant pulses is explained, but not a weak giant population. The power law index derived also has implications in the interpretation of giant pulse emission on the basis of self organized criticality (Bak et al. 1987) suggested by Cairns (2004).

The spectral index of the Crab giant pulses reported in this work suggests that the emission bandwidth is at least $\Delta\nu/\nu > 0.1$ and may approach the upper limit $\Delta\nu/\nu = 0.2$ predicted in numerical models by Weatherall (1998). Hankins & Eilek (2007) found a similar emission bandwidth at 9.5 GHz. Moreover, the average spectral index of giant pulses at the interpulse phase is flatter than the giant pulses at the main pulse phase. This possibly explains the dominant and bright nature of interpulse giants at $\nu > 5$ GHz. We note the prominent emergence

of bimodality in the intensity distribution of the interpulses relative to the main phase pulses. Furthermore, (Hankins & Eilek 2007) found upward drifting emission bands in the spectrum of the interpulses giants and not in the main pulse giants. These differences strongly suggests a different nature to the interpulses. To explain the drifting emission bands, Lyutikov (2007) derived an excess plasma density of $\sim 10^5$ and a large Lorentz factor of the emitting particles on the order of $\sim 10^7$ and this condition is satisfied close to the light-cylinder over the magnetic equator. However, the model proposed by Lyutikov (2007) is only valid for $\nu > 5$ GHz, where the emission bands are observed. While results from our observations cannot support or rule out this model, the difference in pulse intensity distributions we find indicates that the interpulse giants are different in nature.

It is worth noting that the pulsar signal is a stochastic process that contributes to the measurement noise of the pulsed intensity. This is especially true in the case of giant pulse emission, where pulsed flux can exceed 1500 Jy, an order of magnitude greater than the system equivalent flux density (SEFD) of approximately 145 Jy. Source-intrinsic noise increases the measurement uncertainty of various derived parameters, such as the pulsed flux density, pulse width, scattering time, and spectral index (van Straten 2009). In addition, any temporal and/or spectral correlations – either intrinsic to the giant pulse emission or induced by interstellar scintillation – will also affect the uncertainties of any derived parameters. The vast majority of the pulses presented in this analysis have average flux densities smaller than the SEFD, and we do not expect that self-noise will significantly alter the results of this analysis. To accurately quantify the impact of self-noise on parameter distributions (such as those presented in Figures 4,5,7, and 8) would require extensive simulations that are beyond the scope of the present work but may provide additional insights in a future chapter.

The previously unreported double pulses we found are consistent with the occurance rate on a purely problistic basis. Collecting even more of these pulse pairs would allow for better checks of the statistics of occurance to check that they are chance occurances and not indicative of some longer term underlying phenomenon driving the giant pulse emission. Moreover detecting more of these pulses at higher time resolution would provide further insight into the nature of these pulses. Hankins & Eilek (2007) found that the giant pulses at the interpulse phase show an additional dispersion when compared to the pulses at the main pulse phase. The closest pulse pair they were able to examine were separated by 12 minutes. Therefore, one may gain new insights into the excess dispersion seen at the interpulse phase by examining the double giant pulses, which are the closest giant pulse pairs possible. This analysis was not possible in the current work due to insufficient time resolution.

Scattering analysis of single pulses presented in this chapter show a variety of scattering times and corroborates with the analysis of Sallmen et al. (1999). They show that scattering due to multiple screens, or a single thick screen, is excluded because of the observed frequency independence of the pulse component separation. From this it was concluded that the multiple components that make up the giant pulses are intrinisic to the emission mechanism. Using multiple components and the double pulses, we measured scintillation timescales greater than 14 ms which indicates that there are no large changes in the number density of the scattering particles along the line of sight through the Nebula on similar timescales. The fact that the multiple components we detect in the giant pulses are spaced by at least 25 μs

implies that the magnetosphere and/or the plasma does not change on these timescales, if the source intrinsic emission is less than 25 μs. On the other hand, giant pulses may consist of overlapping nano shots. In this case the competing models make use of plasma turbulance leading to modulational instablity (Weatherall 1998) or the induced Compton scattering of low frequency radio waves (Petrova 2004) in the magnetosphere to explain the origin of the nano shots. While with our data we are not sensitive to the pulses less than 4.1 μs, there is an indication that the emission bandwidth $\Delta\nu/\nu > 0.1$ suggesting that the pulses can potentially have structure as narrow as 3.6 ns at this frequency.

3.8 Conclusions

The large collection of single pulses we have gathered have allowed us to perform a range of statistics with the data. After careful flux calibration, a detailed analysis of the pulse intensities, energies, widths and separation times was done by computing distributions of these quantities. In the single pulse intensity distributions, we find a clear evidence for two distinct populations in the giant pulses. The giant pulse separation times show a Poission distribution, and the rate of occurance of giant pulses was determined. Spectral indices for a large number of giant pulses were computed with the narrowly spaced multi band data. Significant dispersion in the spectral indicies was found and a small negative average spectral index was found for the main and interpulse giants, and they are flatter than the average pulse emission. We also note that in some cases there is evidence for intensity modulation with bandwidths which are smaller than the full band but not consistent with scintillation effects. The previously undetected double giant pulses were presented for the first time and we find that they are not more frequent than would be expected by chance. The scatter time for a large number of giant pulses was determined by modelling the scatter broadening as an exponenial function and the distribution of scatter times was computed. Using multiple emission components either at the main or interpulse phase and the double giant pulses, we find no evidence for variation of the scattering material on timescales shorter than 14 ms based on the correlation coefficient computed for emission within a single pulse period.

3.9 Acknowledgements